High Power Laser Science and Engineering, (2024), Vol. 12, e48, 7 pages.
doi:10.1017/hpl.2024.30

HIGH POWER LASER
SCIENCE AND ENGINEERING

RESEARCH ARTICLE

High-efficiency, high-resolution multiple monochromatic imaging based on a multilayer mirror array for laser–plasma diagnostics of X-ray continuum emission

Tongzhou Li[1,2], Huiyao Du[1,2], Zhong Zhang[1,2], Zhe Zhang[1,2], Qiushi Huang[1,2,4], Shengzhen Yi[1,2],
Zhanshan Wang[1,2], Wei Wang[3], and Jinren Sun[1,2,3]

[1] *MOE Key Laboratory of Advanced Micro-Structured Materials, Tongji University, Shanghai, China*
[2] *School of Physics Science and Engineering, Tongji University, Shanghai, China*
[3] *Shanghai Institute of Laser Plasma, CAEP, Shanghai, China*
[4] *Zhejiang Tongyue Optical Technology Co., Ltd., Huzhou, China*

(Received 18 March 2024; revised 27 April 2024; accepted 17 May 2024)

Abstract

The measurement of X-ray continuous emission from laser-driven plasma was achieved through multiple monochromatic imaging utilizing a multilayer mirror array. This methodology was exemplified by the development of an eight-channel X-ray imaging system, capable of operating in the energy range of several keV with a spatial resolution of approximately 3 μm. By integrating this system with a streak camera, the temperature and trajectory of imploding capsules were successfully measured at the kJ-class Shenguang III prototype laser facility. This approach provides a synchronous diagnostic method for the spatial, temporal and spectral analysis of laser-driven plasma, characterized by its high efficiency and resolution.

Keywords: high resolution; multilayer mirror array; multiple monochromatic imaging; plasma diagnostics; X-ray continuum emission

1. Introduction

The measurement of continuous X-ray emission from laser-driven plasma plays a crucial role in acquiring plasma information. This method becomes particularly effective at high X-ray energies, allowing for the deduction of electron temperature by analyzing the intensity ratio of the continuous spectrum independently of the electron density. Its application spans various domains of inertial confinement fusion, including laser fusion and Z-pinch, as well as magnetic confinement fusion[1–3]. Current methodologies predominantly comprise transmission-type Ross filters[4] and diffraction-type gratings or crystals used in spectroscopy[5–8]. While Ross filters are simple and reliable, they offer limited spectral resolution. Conversely, diffraction-based methods provide high spectral resolution and an extensive dataset for analysis but struggle to deliver spatial resolution and are hampered by low signal intensity. Consequently, these methods are less effective in scenarios characterized by weak X-ray radiation or low electron temperatures.

The multiple monochromatic imager, another diffraction-based, multispectral imaging approach, has seen deployment at the US OMEGA laser facility[9,10]. This method involves the initial imaging of continuous X-ray emissions through a pinhole array, followed by the selection of specific X-ray energies via a multilayer mirror, and the eventual capture of these monochromatic X-ray images by time-gated microchannel plate detectors. This technique enables the extraction of spatially resolved spectral data, facilitating the analysis of electron temperature and density across different spatial and temporal dimensions. However, the limited pinhole aperture size results in low collection efficiency (approximately 10^{-8} sr) and poor spatial resolution (10–20 μm), making it a challenge to balance the signal-to-noise ratio with spatial resolution for diagnostic purposes. Thus, its use is mainly confined to the diagnostics of X-ray characteristic lines from doped elements[11,12]. Given the rapid and significant variations in the temperature

---

Correspondence to: S. Yi, MOE Key Laboratory of Advanced Micro-Structured Materials, Tongji University, Shanghai 200092, China. Email: 023123@tongji.edu.cn; W. Wang, Shanghai Institute of Laser Plasma, CAEP, Shanghai 201800, China. Email: wei_wang@fudan.edu.cn; J. Sun, School of Physics Science and Engineering, Tongji University, Shanghai 200092, China. Email: sunjinren@263.net

distribution of laser-driven plasma, a method that can more effectively measure X-ray continuous emission from plasmas, especially in the absence of dopant elements where X-ray emission is weak, becomes imperative.

This study introduces a novel multiple monochromatic imaging technique based on a multilayer mirror array designed for the diagnostics of X-ray continuous emission within the energy range of several keV. By employing grazing-incidence reflection to focus X-rays, this method surpasses pinhole imaging in spatial resolution, achieving 3–5 μm, and in collection efficiency, reaching 10^{-7}–10^{-6} sr[13,14]. This represents a significant advancement over previous X-ray multilayer systems[15,16], extending the operational energy range to several keV and increasing the number of energy points from two to four. This approach facilitates the comprehensive acquisition of plasma information across spatial, temporal and spectral dimensions. An eight-channel X-ray focusing imaging system, operational at four energy points (2.6, 3.1, 3.7 and 4.3 keV), was developed based on this method. By integrating this system with a streak camera, the paper successfully demonstrates the application of multiple monochromatic imaging diagnostics on imploding capsules. The subsequent sections will detail the optical and multilayer design, system assembly and adjustment and experimental results obtained at the Shenguang III prototype laser facility[17].

2. Working principle

The X-ray focusing imaging system developed in this study is designed to capture time-evolving images of plasma spontaneous radiation across four energy channels (2.6, 3.1, 3.7 and 4.3 keV), as well as time-integrated information such as hot spot shapes and implosion symmetry. To meet these requirements, the system is configured to acquire eight images, with two images simultaneously captured at each energy level. One image is dedicated to time-evolution imaging, and the other to time-integrated imaging. Figure 1 presents the overall configuration of the proposed system, where each set of the multilayer mirror array comprises one total reflection spherical mirror (TRM1/TRM2) and four spherical multilayer mirrors (M1–M4) positioned sequentially along the optical axis. A single wide-spectrum TRM (either TRM1 or TRM2) is used for focusing in the meridional direction across all energy channels, while distinct spherical multilayer mirrors are utilized for spectral selection and focusing in the sagittal direction for each channel. This arrangement of spherical mirrors facilitates high-efficiency and high-resolution X-ray imaging, with spectral selection achieved through four different multilayers coated on mirrors M1–M4. This design significantly improves collection efficiency by one to two orders of magnitude over pinhole imaging, while maintaining a higher spatial resolution of 3–5 μm, and efficiently maps various image points onto a time-resolved recording device, such as a streak camera.

To ensure consistent spatial orientation of the mirror array, given the significant variation in spatial resolution of grazing-incidence X-ray imaging with the field of view (FOV), three precision-machined reference cores were utilized, as depicted in Figure 1. The six mirrors are arranged in pairs, each aligned closely with a reference core. For the 3.7/4.3 keV energy channels, larger diameter mirrors (M1 and M2) are chosen to boost collection efficiency in the higher energy spectrum. The two total reflection mirrors (TRM1 and TRM2) each generate two columns of images, which are synchronously recorded with a streak camera and an image plate (IP) for concurrent time-resolved and time-integrated measurements.

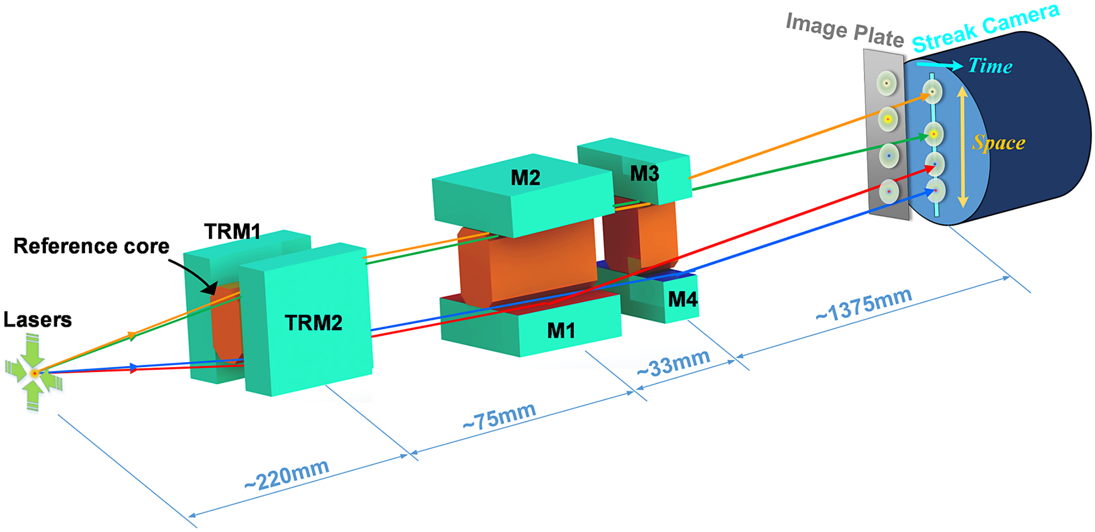

Figure 1. Schematic representation of the high-efficiency, high-resolution multiple monochromatic imaging system using a multilayer mirror array.

Following the finalization of the optical schematic, the grazing angle (θ) for each spherical mirror was determined to ensure that the multilayers reflect X-rays at their respective working energies, while also reflecting the Cu Kα characteristic line (8.048 keV) for experimental assembly in an air environment using a common Cu X-ray tube. For example, TRM1 and TRM2, which primarily function at four energies, utilize multilayer coatings to reflect X-rays at 8.048 keV. Based on the total reflection condition, the grazing angles for TRM1 and TRM2 are set at 0.95°. Table 1 lists the final optical parameters of the system, including the curvature radius (R) designed to satisfy the imaging relationship shown in Equation (1) for each channel:

$$\frac{1}{u}+\frac{1}{v}=\frac{1}{f}=\frac{2}{R\sin\theta}, \tag{1}$$

where u and v represent the object and image distances, respectively, and f denotes the focus distance. The mirror lengths (d) of M1 and M2 for the 3.7 and 4.3 keV energy channels are set at 30 mm to enhance collection efficiency for the higher X-ray energy range.

The system developed in this study is tailored for spontaneous imaging of X-ray emission from laser-driven plasmas at four specific energies: 2.6, 3.1, 3.7 and 4.3 keV. To ensure consistent intensity across the plasma evolution images, two sets of multilayer coatings, each operating at different grazing angles, are engineered to possess nearly identical reflectivity. The upper multilayers, designed for high reflectivity at their respective working energies, utilize Ru/C materials for the low-energy channels (below 3 keV) and WC/SiC for the high-energy channels (above 3 keV). The lower multilayers, aimed at reflecting X-rays at 8.048 keV, employ a WC/SiC periodic multilayer stack. In addition, a single-layer structure comprising W and Ni is implemented in TRM1 and TRM2 to facilitate high-efficiency total reflection of X-rays below 4.3 keV. The selection of these four energies is strategic, as they are proximal to the Kα line of Cl (2.6 keV), and the helium-like lines of Ar and Sc (3.1 and 4.3 keV), making them suitable for imaging diagnostics of these characteristic lines.

The multilayers were deposited on ultra-smooth silicon spherical mirrors using direct current (DC) magnetron sputtering. Mirror surface roughness, measured with an atomic force microscope (AFM) (Bruker Dimension Icon), was maintained below 0.3 nm. The reflectivity curves of the multilayers at the Cu Kα line (8.048 keV) were assessed using an X-ray diffractometer (Bruker D8 plus). The multilayer parameters, including thickness, density and interface width, were deduced by fitting the measurement data through the genetic algorithm[18] with Bede REFs software[19], as detailed in Table 2. Here, the symbol γ represents the ratio of the absorber layer (W, Si, Ru and C) thickness to the overall period thickness. The energy response of the five spherical mirrors, based on the parameters outlined in Table 2, is depicted in Figure 2.

Table 1. Optical parameters of the eight-channel X-ray focusing imaging system.

Mirror	E (keV)	θ	R (m)	u (mm)	v (mm)	M	d (mm)
TRM1/2	<4.3	0.950°	23.0	218.7	1481.3	6.773	30
M1/M2	4.3/3.7	1.320°	21.0	292.1	1407.9	4.821	30
M3/M4	3.1/2.6	1.440°	21.0	325.3	1374.7	4.297	10

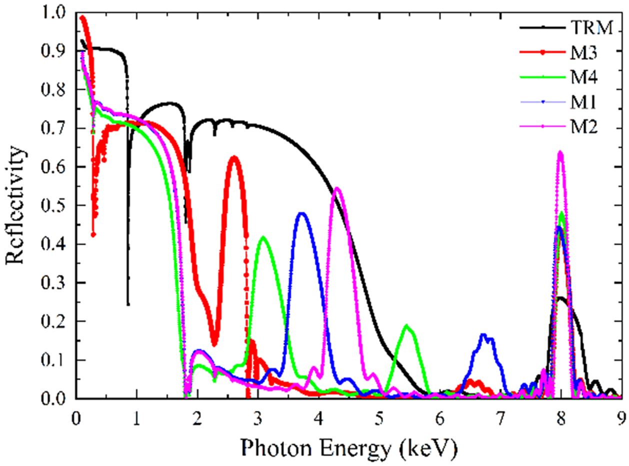

Figure 2. Energy response curves for five spherical mirrors, determined through X-ray diffractometer measurements.

Table 2. Fitted multilayers parameters of M1–M4 by X-ray diffractometer measurement.

Mirror	Energy (keV)	Material	Period number	Period thickness
TRM1/2	<4.3	W + Ni	1	20 nm + 3 nm
	8	WC/SiC	25	$d = 5.05$ nm, $\gamma = 0.45$
M1	3.7	WC/SiC	6	$d = 8.45$ nm, $\gamma = 0.30$
	8.048	WC/SiC	40	$d = 3.51$ nm, $\gamma = 0.45$
M2	4.3	WC/SiC	10	$d = 7.00$ nm, $\gamma = 0.30$
	8.048	WC/SiC	40	$d = 3.51$ nm, $\gamma = 0.45$
M3	2.6	Ru/C	3	$d = 12.10$ nm, $\gamma = 0.50$
	8.048	WC/SiC	40	$d = 3.19$ nm, $\gamma = 0.45$
M4	3.1	WC/SiC	3	$d = 9.67$ nm, $\gamma = 0.30$
	8.048	WC/SiC	40	$d = 3.19$ nm, $\gamma = 0.45$

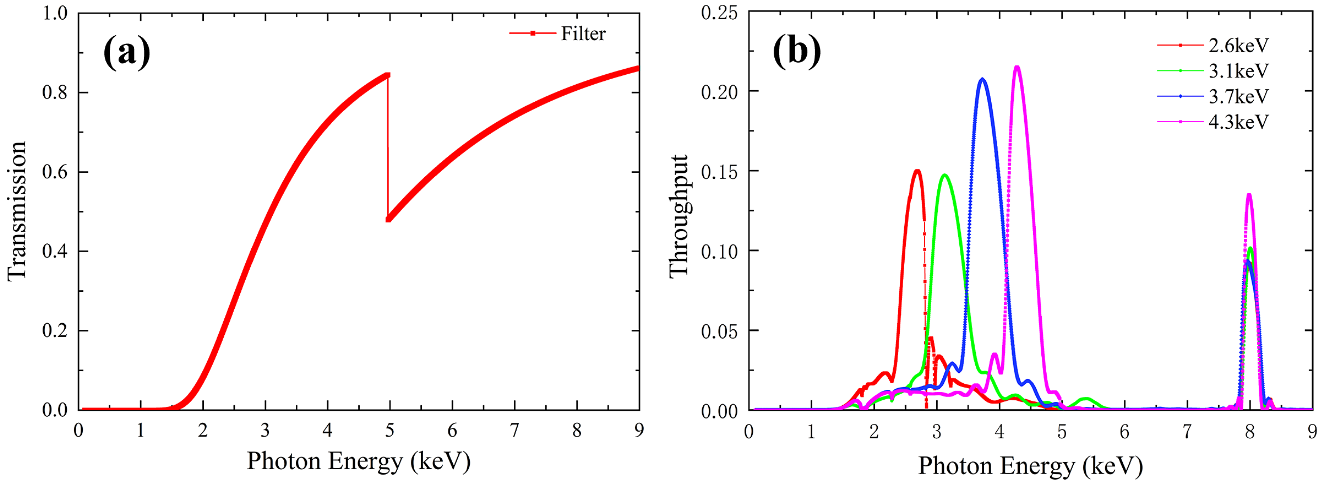

Figure 3. (a) Variation in filter transmittance with X-ray energy. (b) Combined transmittance curves of the four imaging channels across the X-ray energy spectrum.

In addition, to ensure that each imaging channel receives only quasi-monochromatic responses, it is crucial to employ X-ray filters to suppress low-energy rays and certain higher harmonic reflections. In this study, the selected filter combination includes 10 μm of CH, 100 μm of Be and 2 μm of Ti. The transmission curve, as a function of X-ray energy, is depicted in Figure 3(a). The Be filter efficiently attenuates X-rays below 2 keV but is less effective at higher energies, while the Ti filter exhibits an absorption edge near 5 keV. The filter was placed in front of mirrors TRM1/TRM2 to avoid contamination and damage by the debris. Moreover, total reflection mirrors TRM1 and TRM2 are capable of filtering out high-energy X-rays. By integrating these components, the system can effectively eliminate both low- and high-energy X-rays, thereby enhancing the monochromaticity of the imaging process. Figure 3(b) shows the combined transmission curve of four energy channels for the streak camera across the X-ray energy spectrum. Calculations indicate that the energy bandwidth is approximately 385 eV at 2.6 keV, 580 eV at 3.1 keV, 572 eV at 3.7 keV and 440 eV at 4.3 keV. In addition, a 10 μm Al filter was superimposed before the time-integrated IP to suppress brightness overexposure.

3. System assembly

The spatial resolution of X-ray grazing imaging optics decreases rapidly with the deviation from the central FOV. To obtain optimal spatial resolution, all mirrors of the developed system must be accurately aimed at the central FOV. Due to the diffraction effect of the grazing-incidence imaging on visible light, the system assembly must be completed in the X-ray energy range. In this paper, it was completed by the imaging experiment of a metal grid using a common copper X-ray tube (8.05 keV, Cu Kα line) in an air environment. The experiment employed a 600-mesh Au grid with a period of 42 μm and line widths ranging from 5 to 6 μm. A marker hole with a diameter of 120 μm was predrilled on the grid to serve as an object position reference. An X-ray charge-coupled device (CCD; Photonic Science VHR-11M) with pixel dimensions of 9 μm × 9 μm was positioned

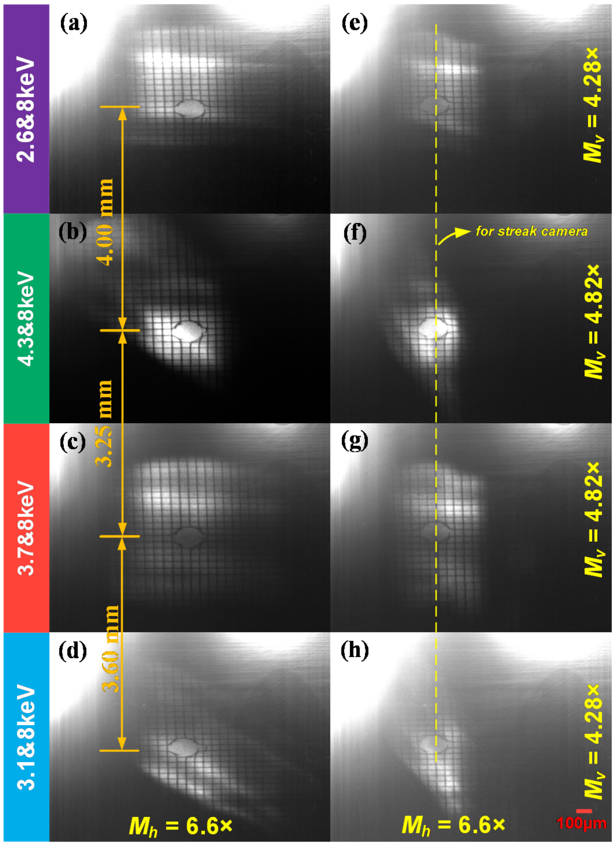

Figure 4. Calibration outcomes of the high-efficiency, high-resolution multiple monochromatic imaging system, demonstrating its performance across four energies after assembly.

on the image plane to capture the imaging result for each channel. After careful adjustment of all mirrors, eight images were obtained in sequence after 10 minutes of exposure, as illustrated in Figures 4(a)–4(g). The operating voltage and current of the copper X-ray tube are 35 kV and 20 mA, respectively. The spatial resolution was evaluated using the '10%–90%' intensity peak-to-valley change criterion near the grid edges[20], yielding an optimal spatial resolution of approximately 3 μm in the central FOV for each channel, while the spatial resolution within a ±100 μm FOV exceeded 5 μm. The center marker holes of the four images in Figures 4(e)–4(h) were arranged in a strict straight line with a two-pixel deviation, which indicated the alignment accuracy of approximately 3 μm for the same object FOV, and thus these four channels were used to couple with the streak camera to acquire a 1D, time-resolved image. At this time, the image spacing was 4.0 mm between 2.6 and 4.3 keV, 3.25 mm between 4.3 and 3.7 keV and 3.6 mm between 3.7 and 3.1 keV. The other four channels corresponding to Figures 4(a)–4(d) were used for time-integrated signal acquisition.

4. Online experiment

The four-energy, eight-channel X-ray imaging system was developed for diagnostic experiments at the Shenguang III prototype laser facility. The system's mechanical structure, depicted in Figure 5, was designed to facilitate its connection to the facility chamber and the installation of image recording components. The main flange was first connected to the facility chamber, followed by the attachment of an object point indicator, a ball with a diameter of 300 μm, to the multilayer mirror array. The ball's center was calibrated to align with the position of the marker hole. Before the diagnostic experiments, the ball center could be precisely aligned using the target viewing system in the laser facility. A visible CCD was then rigidly connected to the multilayer mirror array, enabling accurate positioning of the four image coordinates, as shown in Figure 5(b). This setup ensured precise alignment between the four image points and the photocathode of the streak camera, facilitating rapid and accurate positioning of the photocathode. Finally, an IP was placed near the streak camera on the image plane to monitor the hot spot size, shape and whether the streak camera is working properly.

After removing the point indicator, we placed a direct-drive deuterated plastic (CD) shell target on the position of the ball's center to carry out the formal diagnostic experiment. The target shell was made of CD with an outer diameter of $\Phi = 312$ μm and a wall thickness of 19.3 μm, and supported by an Au target rod. Eight laser beams (frequency tripled to 351 nm, 800 J/beam, smoothed with continuous phase plate (CPP) to $\Phi = 500$ μm, four beams per hemisphere, equally distributed in the azimuthal direction, incident angle relative to the vertical axis is 45°) directly illuminated the shell surface.

Time-resolved images of X-ray self-emission from the target at energies of 2.6, 3.1, 3.7 and 4.3 keV were captured by the streak camera, as shown in Figure 6(a). The time evolution of self-emission intensity from the CD shell target at these four energies was clearly observable. Initially, the shell surface began emitting X-rays due to laser irradiation, and as the shell underwent inward compression, the central temperature increased, resulting in further emission. The multilayer mirrors of 2.6 and 3.1 keV have the same mirror length of 10 mm, but since the self-emission intensity gradually decreases as the X-ray energy increases, the image brightness for the 3.1 keV channel was significantly weaker than for that at 2.6 keV. Despite being at a higher energy, the 3.7 and 4.3 keV channels still achieve image brightness higher than that of 2.6 keV, mainly due to the longer mirror length of 30 mm.

The time-integrated image recorded on the IP is presented in Figure 6(b). Due to the additional use of a 10 μm Al filter to suppress overexposure, the image brightness of the two low-energy channels is significantly lower than that of the high-energy channels. According to the integrated image of the high-energy channels, the center hotspot has a good symmetry, indicating that the target shell was uniformly compressed.

From the time-resolved images of X-ray self-emission in Figure 6, further insights into the evolution of the high-intensity emission regions on the shell surface can be

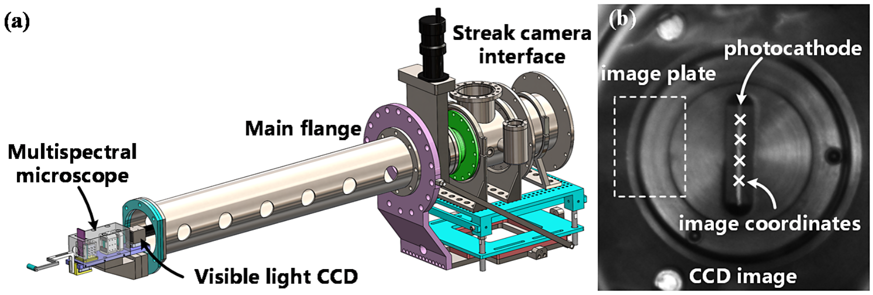

Figure 5. (a) Diagram showing the mechanical setup of the imaging system. (b) Method used for precise alignment of the streak camera's photocathode using an online aiming technique.

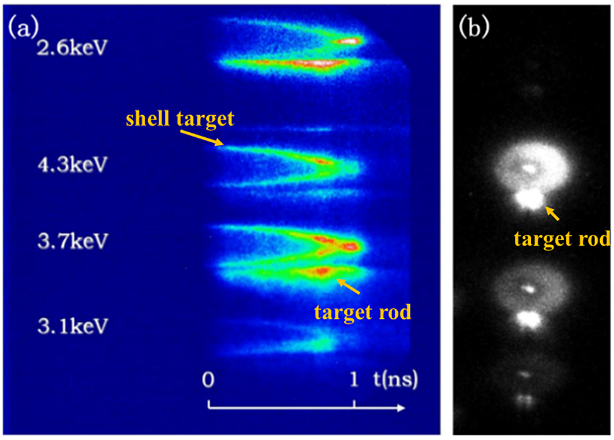

Figure 6. Imaging results capturing X-ray self-emission from a direct-drive CD shell target at four energies: (a) captured using a streak camera; (b) recorded on an image plate.

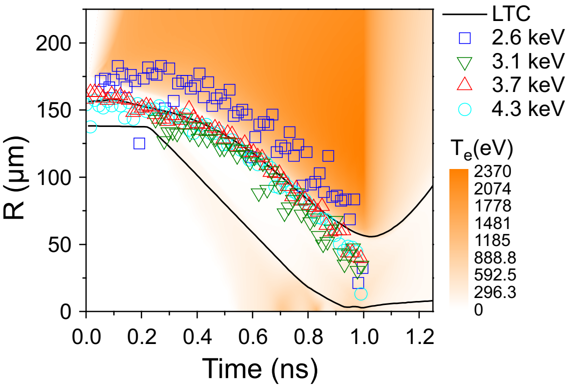

Figure 7. Time-dependent variations in self-emission intensity at four energies from a direct-drive CD shell target.

gleaned, as illustrated with the marked symbols in Figure 7. Due to lower signal-to-noise ratio, the calibrated data points of the two low-energy channels at different times differ from those of the two high-energy channels. A 1D hydrodynamic code laser–target coupling (LTC)[21,22] was used to simulate the imploded shell radius R and electron temperature T_e evolving with time under the current laser and target parameters, where solid lines represent the shell surfaces and the color map shows the electron temperature. The figure visually represents the changes in temperature and implosion trajectory over time near the critical density surface. It is observed that there are obvious differences in the spatial distribution for different self-emission X-ray energies. The experimental measurements of the high-energy emission regions (3.7 and 4.3 keV) are in good agreement with the implosion trajectory predicted by theoretical simulations. The measurement results in the low-energy regions (2.6 and 3.1 keV) are somewhat different from the simulation, requiring further theoretical analysis. It also illustrates the significance of the system developed in this paper.

5. Summary

This study introduces a high-efficiency, high-resolution multiple monochromatic imaging system for X-ray continuous self-emission diagnostics utilizing a multilayer mirror array. An eight-channel X-ray imaging system has been designed and developed for energies of 2.6, 3.1, 3.7 and 4.3 keV, achieving a spatial resolution of approximately 3–5 μm. In conjunction with a streak camera, diagnostic experiments were conducted to analyze the temperature and implosion trajectory near critical density surfaces of a CD imploding target at the kJ-class Shenguang III prototype facility. Compared with the previous similar system[13,14], the multilayer mirror array developed in this paper has nearly an order of magnitude improvement in collection efficiency while maintaining a spatial resolution of 3–5 μm. This system is capable of acquiring spatial, temporal and spectral information from weak and small-scale X-ray signals during implosion, offering easily adjustable response energies with excellent scalability. This provides a novel approach for diagnosing plasma parameters in the core region of inertial confinement fusion.

Acknowledgements

This work was supported by the National Key Research and Development Program (Grant No. 2019YFE03080200) and the National Natural Science Foundation of China (Grant No. 12204353).

References

1. B. Jones, C. Deeney, J. L. McKenney, D. J. Ampleford, C. A. Coverdale, P. D. Lepell, K. P. Shelton, A. S. Safronova, V. L. Kantsyrev, G. Osborne, V. I. Sotnikov, V. V. Ivanov, D. Fedin, V. Nalajal, F. Yilmaz, and I. Shrestha, Phys. Rev. Lett. **100**, 105003 (2008).
2. C. Deeney, J. P. Apruzese, C. A. Coverdale, K. G. Whitney, J. W. Thornhill, and J. Davis, Phys. Rev. Lett. **93**, 155001 (2004).
3. E. L. Dewald, O. L. Landen, L. J. Suter, J. Holder, K. Campbell, S. H. Glenzer, J. W. McDonald, C. Niemann, A. J. Macknnon, M. S. Schneider, C. Haynam, D. Hinkel, and B. A. Hammel, Phys. Plasmas **13**, 056315 (2006).
4. L. Yao, Y. Pu, X. Zhan, M. Wei, J. Zheng, X. Zhang, J. Yan, L. Hou, Y. Yang, and Y. Ding, High Energy Density Phys. **37**, 100882 (2020).
5. S. Z. Yi, J. Q. Dong, L. Jiang, Q. Huang, E. Guo, and Z. Wang, Matter Radiat. Extremes **7**, 015902 (2022).
6. M. Bitter, K. W. Hill, B. Stratton, A. L. Roquemore, D. Mastrovito, S. G. Lee, J. G. Bak, M. K. Moon, U. W. Nam, G. Smith, J. E. Rice, P. Beiersdorfer, and B. S. Fraenkel, Rev. Sci. Instrum. **75**, 3660 (2004).
7. S. Yi, H. Du, H. Si, Z. Zhou, L. Jiang, Z. Wang, and R. Cheng, Nucl. Instrum. Methods Phys. Res. Sect. A **1057**, 168722 (2023).
8. E. C. Harding, T. Ao, J. E. Bailey, G. Loisel, D. B. Sinars, M. Geissel, G. A. Rochau, and I. C. Smith, Rev. Sci. Instrum. **86**, 043504 (2015).
9. C. Burcklen, J. von der Linden, A. Do, B. Kozioziemski, M.-A. Descalle, and H. Chen, Revi. Sci. Instrum. **92**, 035105 (2021).

10. L. A. Welser, R. C. Mancini, J. A. Koch, S. Dalhed, R. W. Lee, I. E. Golovkin, F. Marshall, J. Delettrez, and L. Klein, Rev. Sci. Instrum. **74**, 1951 (2023).
11. H. Sawada, Y. Sentoku, T. Yabuuchi, U. Zastrau, E. Förster, F. N. Beg, H. Chen, A. J. Kemp, H. S. McLean, P. K. Patel, and Y. Ping, Phys. Rev. Lett. **122**, 155002 (2019).
12. D. T. Cliché and R. C. Mancini, Appl. Opt. **58**, 4753 (2019).
13. S. Yi, F. Zhang, Q. Huang, L. Wei, Y. Gu, and Z. Wang, High Power Laser Sci. Eng. **9**, e42 (2021).
14. S. Yi, H. Si, K. Fang, Z. Fang, J. Wu, R. Qi, X. Yuan, Z. Zhang, and Z. Wang, J. Opt. Soc. Am. B **39**, A61 (2022).
15. S. Yi, B. Mu, J. Zhu, X. Wang, W. Li, Z. Wang, P. He, W. Wang, Z. Fang, and S. Fu, Chin. Opt. Lett. **12**, 083401 (2014).
16. W. Wang, Z. Fang, G. Jia, S. Yi, Y. Tu, J. Zhu, B. Mu, H. An, R. Wang, Z. Xie, J. Ye, X. Meng, H. Zhou, C. Wang, A. Lei, Z. Wang, and S. Fu, Eur. Phys. J. D **68**, 129 (2014).
17. S. Jiang, F. Wang, Y. Ding, S. Liu, J. Yang, S. Li, T. Huang, Z. Cao, Z. Yang, X. Hu, W. Miao, J. Zhang, Z. Wang, G. Yang, R. Yi, Q. Tang, L. Kuang, Z. Li, D. Yang, and B. Zhang, Nucl. Fusion **59**, 032006 (2018).
18. M. Wormington, C. Panaccione, K. M. Matney, and D. K. Bowen, Philos. Trans. Roy. Soc. London Ser. A **357**, 2827 (1999).
19. Z. Wei, Z. Zhang, L. Jiang, Y. Yang, C. Chang, Y. Feng, R. Qi, Q. Huang, W. Yan, C. Xie, and Z. Wang, Front. Phys. **10**, 837819 (2022).
20. S. W. Smith, in *The Scientist and Engineer's Guide to Digital Signal Processing* (California Technical Publishing, 1997), p. 423.
21. G. Chen, T. Chang, J. Zhang, X. Zhang, W. Pei, and X. You, Chin. J. Comput. Phys. **15**, 27 (1998).
22. S. Zhu and P. Gu, High Power Laser Part. Beams **11**, 687 (1999).